Contents lists available at AccScience Publishing
Nonlinear Science and Control Engineering (NSCE)
Vol. 2, No. 3 (2026)
https://accscience.com/journal/nsce

Nonlinear pushover analysis of short-column effects induced by different clerestory opening positions in reinforced concrete frames

Mo Shi[1]*, Xinyue Cu[1], and Yeol Choi[2]

[1]*School of Economics and Management, Ankang University, Ankang, China*
[2]*School of Architecture, Kyungpook National University, Daegu, Republic of Korea*

Article History:
Received: July 20, 2026
Revised: August 22, 2026
Accepted: September 1, 2026
Published online: September 18, 2026

A B S T R A C T
The incorporation of clerestory openings in masonry-infilled reinforced concrete (RC) frames is ubiquitous in architectural design for natural ventilation and illumination, but improper design can induce pronounced stiffness irregularities and trigger short column-induced localized damage. This study investigates the sensitivity of the nonlinear seismic performance of masonry-infilled RC frames to the transverse positioning of clerestory openings. Utilizing displacement-controlled nonlinear pushover analysis, four different clerestory opening designs of a one-bay RC frame are evaluated. Plastic-hinge mechanics are defined using the acceptance criteria specified in Seismic Evaluation and Retrofit of Existing Buildings (41-13) (ASCE/SEI 41-13), while capacity–demand equilibria are quantified using the capacity spectrum procedures of Seismic Evaluation and Retrofit of Concrete Buildings (ATC-40) and Improvement of Nonlinear Static Seismic Analysis Procedures (FEMA 440). The findings in this study establish that isolating the clerestory opening from the bounding vertical elements neutralizes captive-column constraints and mitigates premature global stiffness degradation. Specifically, structural configurations featuring internally offset openings demonstrated a 23.36% enhancement in base shear capacity, a 15.77% amplification in energy dissipation, and a 1.62% extension in peak displacement capacity prior to collapse, relative to column-adjacent designs. Furthermore, kinematic damage confirmed that while all structures exhibited a ductile beam-first yielding mechanism, offsetting the fenestrations delayed the propagation of column plastic hinges to higher lateral drift demands. The excellent computational convergence between the ATC-40 and FEMA 440 performance point evaluations also provides a quantitative mechanical foundation and critical theoretical reference for the structural optimization and seismic design of infilled RC infrastructure.

Keywords: Clerestory opening; Short-column effect; Reinforced concrete frame; Nonlinear pushover analysis; Plastic hinge; Seismic performance

1. Introduction

Severe seismic events worldwide have repeatedly underscored the vulnerability of reinforced concrete (RC) structures to localized failure mechanisms, notably in earthquake-prone regions such as Japan and Turkey.[1-4] According to many previous studies, the short-column effect remains a pervasive and critical initiator of catastrophic structural collapse.[5-9] As Zhang *et al.*[10] emphasized, structural collapses due to the short-column effect manifest when the effective shear span of a column is inadvertently constrained by adjacent structural or

***Corresponding author:**
Mo Shi (shimo0204@outlook.jp).

Citation: Shi M, Cu X, Choi Y. Nonlinear pushover analysis of short-column effects induced by different clerestory opening positions in reinforced concrete frames. *Nonlinear Sci Cont Eng*. 2026;2(3):026300032. doi: 10.36922/NSCE026300032

Copyright: © 2026 The Author(s). This is an Open Access article distributed under the terms of the Creative Commons Attribution License, permitting distribution, and reproduction in any medium, provided the original work is properly cited.

non-structural elements, thereby drastically altering its fundamental mechanical behavior. Due to the short-column effect, the constrained column does not develop a ductile flexural-yielding mechanism and is subjected to extreme shear-force concentrations. Consequently, the columns experience brittle shear deterioration, abrupt stiffness degradation, and an ultimate loss of axial load-bearing capacity with minimal early warning. As shown in **Figure 1**, post-earthquake reconnaissance extensively corroborates that such configurations govern the localized damage sequence, rendering the accurate identification and mitigation of short-column effects imperative for enhancing the seismic resilience of RC frames.

In contemporary architectural practice, clerestory openings are extensively integrated into the design of educational facilities, industrial plants, warehouses, and exhibition halls. According to Hammad *et al.*[11], this architectural configuration optimizes deep natural daylight penetration, preserves valuable lower wall space for functional utility (e.g., equipment installation and exhibition arrangements), and ensures indoor privacy by situating windows along the uppermost section of a wall. As shown in **Figure 1**, despite these profound architectural merits, incorporation of clerestory openings inevitably introduces severe discontinuities within the frame–infill interactive system. The remaining partial-height masonry infill acts as a rigid restraint against the adjacent RC columns, significantly curtailing their deformable length and inducing the short-column anomaly. Under lateral seismic excitation, the constrained segment of the column attracts a high shear demand at the opening interface, predisposing the vertical structural elements to premature localized shear failure and threatening the global stability of the structure.

While the detrimental consequences of partial-height infill walls are recognized, recent studies on short-column mechanics[12-14] and seismic vulnerability under damage accumulation[15-17] have highlighted the critical sensitivity of RC frames to structural discontinuities. Furthermore, advancements in nonlinear static pushover evaluation techniques[18-24] emphasize the necessity for precise assessments of localized failures. Despite these advancements, the influence of the positions of lateral clerestory openings on the nonlinear response of RC frames remains underexplored. Previous investigations primarily focused on generalized partial-height infills, theoretical shear models, or retrofitting strategies. However, in practical applications, clerestory window placement is dictated by aesthetic and functional lighting demands rather than seismic optimization. Consequently, varying the lateral position of the clerestory window openings within the same structural bay engenders highly disparate spatial stiffness distributions, load-transfer trajectories, and plastic deformation patterns. As such, establishing a systematic, quantitative investigation of the transverse location of a clerestory opening that governs the severity of the induced short-column effect remains a significant missing link in current performance-based seismic engineering.

Based on the research background, this study proposes a nonlinear pushover assessment to elucidate the mechanical ramifications of varying lateral clerestory opening positions on RC frames. As shown in **Figure 2**, the target RC frame in this study was modeled as a one-bay RC frame extracted from an educational building at Ankang University, featuring a standard story height of 3.6 m and a span of 5.0 m. The structural design and detailing comply with a comprehensive suite of Chinese national standards, including Code for Design of Concrete Structures (GB 50010), Code for Seismic Design of Buildings (GB 50011), Load Code for the Design of Building Structures (GB 50009), Code for Design of Building Foundation (GB 50007), General Code for Concrete Structures (GB 55008), Unified Standard for Design of Civil Buildings (GB 50352), and Construction Standards for Regular Higher Education Institutions (JB 191-2018). To capture authentic nonlinear frame–infill interactions, fired common brick infill walls were incorporated using brick units conforming to the Chinese national standard for fired common bricks (GB/T 5101-2017), and four distinct structural configurations were developed to isolate the opening-position effects. Geometric modeling and spatial building information modeling visualizations were performed using AutoCAD 2006 (AutoDesk, United States of America) and Revit 2025 (Autodesk, United States

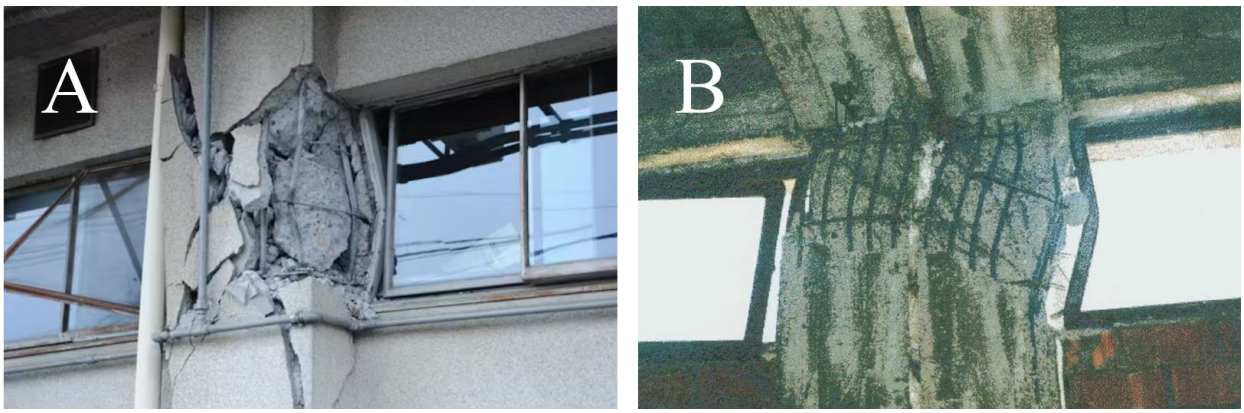

Figure 1. Structural damage from the short-column effect. (A) City hall in Ibaraki (2011). (B) Industrial building in Adana City (1998).

of America), while the nonlinear pushover analysis was performed in SAP2000 (v.22, Computers and Structures Inc., United States of America) and supplemented by MATLAB (R2026b, MathWorks, United States of America) for data post-processing. The evaluation systematically focuses on performance point identification, base shear–displacement capacity, spectral acceleration–spectral displacement characteristics, fundamental period evolution, and plastic hinge developments.

The expected contribution of this study lies in the formulation of a valuable analytical framework that correlates architectural clerestory arrangements with the exacerbation of nonlinear seismic vulnerability. By isolating the spatial variable of the clerestory opening position, this study transcends conventional binary assessments of short columns, offering a perspective on localized stiffness redistribution and damage concentration mechanisms. This study aims to equip structural design with a theoretical basis for evaluating the seismic safety of RC frames with clerestory windows, fostering a synergistic design paradigm that harmonizes specific architectural design requirements with structural resilience and seismic resistance.

2. Descriptions

2.1. Target infilled reinforced concrete frames

Figure 3 delineates the cross-sections and reinforcement detailing of the RC members, including columns and beams, used to construct the representative one-bay frame for nonlinear pushover analysis. To ensure the computational model replicates the structural mechanics of a typical educational RC structure, identical member geometries and reinforcement layouts were applied across all four infilled RC frames. This methodological control ensures that subsequent variations in pushover response are attributable to the topological alterations of the lateral clerestory openings, thereby isolating the short-column phenomenon from any confounding variables related to inherent member capacity or sectional stiffness.

As illustrated in **Figure 3A**, the RC column features a 500 × 500 mm cross-section reinforced with 12 HD19 longitudinal bars and HD10@150 hoops and cross-ties for effective confinement. **Figure 3B** shows the 300 × 600 mm beam section, which incorporates two top and six bottom HD19 longitudinal bars alongside HD10@200 transverse stirrups, satisfying the strong-column–weak-

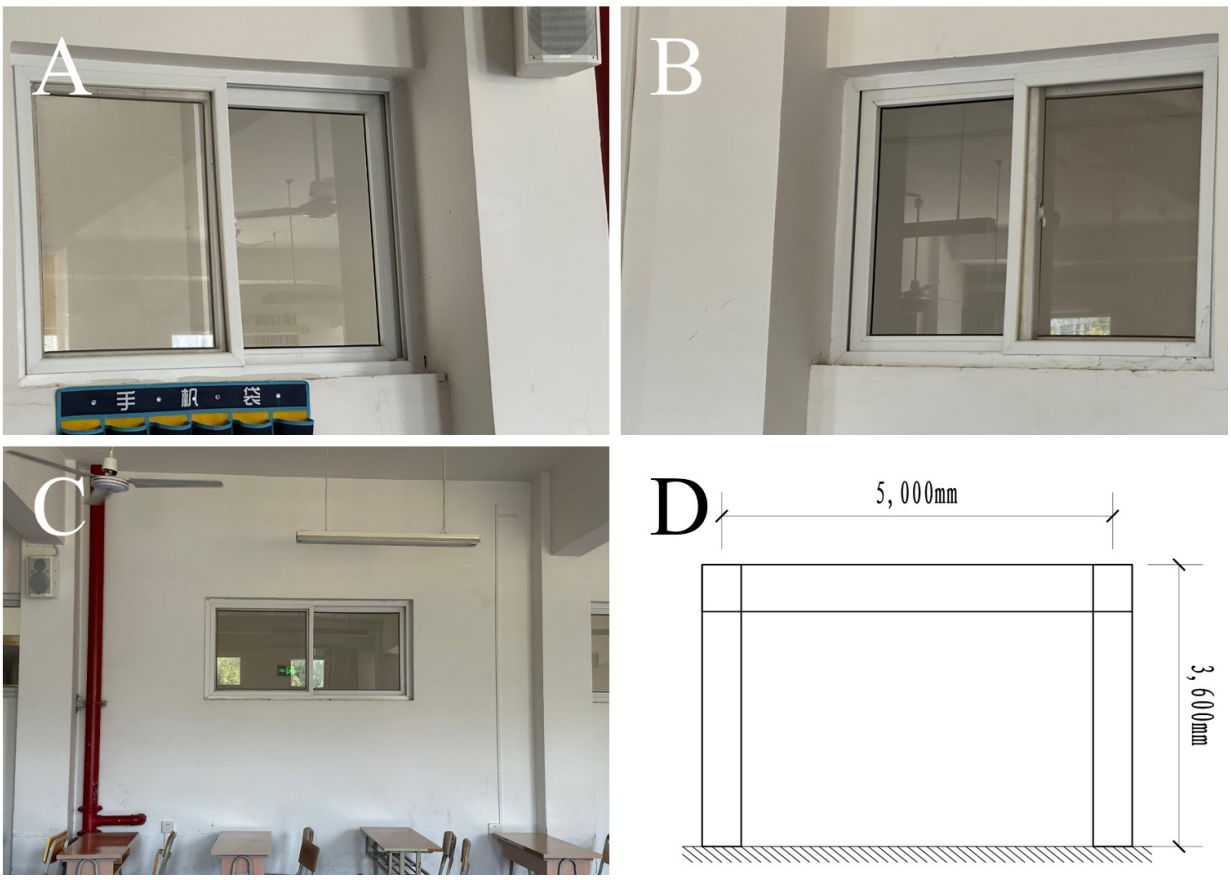

Figure 2. Actual clerestory opening and RC frame details (Ankang University). (A) Clerestory opening on the left. (B) Clerestory opening on the right. (C) Clerestory opening in the middle. (D) One-bay RC frame design.
Abbreviation: RC: Reinforced concrete.

beam philosophy. To evaluate potential shear vulnerability without defining a nonlinear shear hinge, the nominal shear capacity of the column ($\varphi V_n = x\,kN$) was calculated based on the concrete section and transverse reinforcement. Under peak base shear, the maximum shear demand (V_u) at the constrained segment reached $y\,kN$, yielding a demand-to-capacity ratio ($V_n / \varphi V_n$) of z. According to the approach above, the observed mechanism is characterized as short column-induced localized damage and severe stiffness degradation, rather than purely brittle shear failure.

The mechanical properties assigned to the RC members were selected in accordance with GB 50010 to ensure that the material behavior of typical educational RC buildings provides reliable input parameters for nonlinear pushover analysis. As summarized in **Table 1**, the concrete material was assigned a unit weight of 25,000 N/m^3 and a mass density of 2,550 kg/m^3, with an elastic modulus of 30,000 MPa, Poisson's ratio of 0.200, coefficient of thermal expansion of 1.000 × 10^{-5} /°C, and a shear modulus of 12,500 MPa. To capture both nominal and probable structural performance under seismic loading, the concrete compressive strength was defined using a specified compressive strength (f_{ck}) of 20.100 MPa together with an expected compressive strength (f_{ek}) of 25.125 MPa, thereby enabling the nonlinear material model to represent both the design-level resistance and the anticipated in-situ strength characteristics.

Table 1. Concrete property

Property	Value
Weight per unit volume	25,000 N/m^3
Mass per unit volume	2,550 kg/m^3
Modulus of elasticity ($\boldsymbol{E}$)	30,000 MPa
Poisson ($\boldsymbol{\nu}$)	0.200
Coefficient of thermal expansion ($\boldsymbol{\alpha}$)	1.000 × 10^{-5} /°C
Shear modulus ($\boldsymbol{G}$)	12,500 MPa
Specified compressive strength ($\boldsymbol{f_{ck}}$)	20.100 MPa
Expected compressive strength ($\boldsymbol{f_{ek}}$)	25.125 MPa

As shown in **Table 2**, the reinforcement is assigned a weight per unit volume of 77,000 N/m^3, a mass per unit volume of 7,850 kg/m^3, an elastic modulus of 2.00 × 10^5 MPa, a Poisson's ratio of 0.30, and a coefficient of thermal expansion of 1.17 × 10^{-5}/°C. Additionally, the reinforcement model defines a characteristic yield strength ($\boldsymbol{f_{yk}}$) of 400 MPa and a characteristic ultimate tensile strength ($\boldsymbol{f_{stk}}$) of 540 MPa, alongside an expected yield strength ($\boldsymbol{f_{ym}}$) of 440 MPa and an expected ultimate tensile strength ($\boldsymbol{f_{stm}}$) of 590 MPa.

Table 2. Rebar property

Property	Value
Weight per unit volume	77,000 N/m^3
Mass per unit volume	7,850 kg/m^3
Modulus of elasticity ($\boldsymbol{E}$)	2.00 × 10^5 MPa
Poisson ($\boldsymbol{\nu}$)	0.30
Coefficient of thermal expansion ($\boldsymbol{\alpha}$)	1.17 × 10^{-5} /°C
Characteristic yield strength ($\boldsymbol{f_{yk}}$)	400 MPa
Characteristic ultimate strength ($\boldsymbol{f_{stk}}$)	540 MPa
Expected yield strength ($\boldsymbol{f_{ym}}$)	440 MPa
Expected ultimate strength ($\boldsymbol{f_{stm}}$)	590 MPa

To simulate frame–infill interactions, the masonry infill—constructed from MU25 fired clay bricks (240 mm × 115 mm × 53 mm; density of 1835 kg/m^3, elastic modulus of 30,000 MPa, Poisson's ratio of 0.06, thermal expansion coefficient of 5 × 10^{-6}/°C)—was modeled using the concentric equivalent diagonal strut method from Seismic Evaluation and Retrofit of Existing Buildings (41-13) (ASCE/SEI 41-13). The strut width w can be calculated as follows:

$$w = 0.175\left(\lambda_1 h\right)^{-0.4} \cdot r_{inf} \tag{1}$$

where λ_1 represents the relative frame-to-infill stiffness coefficient, h is the frame height, and r_{inf} is the diagonal length. The strut's axial response follows a nonlinear compressive stress-strain constitutive relationship with an ultimate compressive strength of masonry f'_{ms} = 25.0 MPa and a post-peak strength drop at 1.5% strain to represent masonry crushing and interface contact loss.

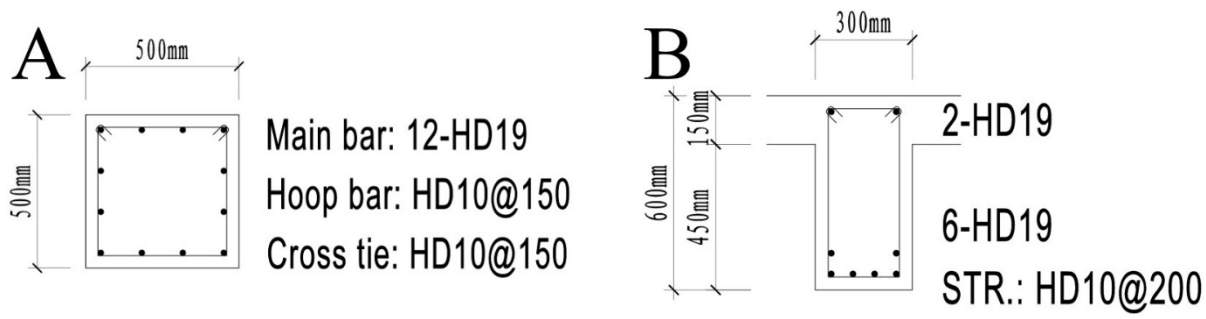

Figure 3. Cross-section design of (A) column and (B) beam
Abbreviation: STR.: Stirrups

To elucidate the mechanical influence of transverse clerestory opening on the exacerbation of short-column effects, four infilled one-bay RC frame configurations were formulated, as delineated in **Figure 4**. The RC frame comprises a 5,000 mm span and a 3,600 mm story height, while the clerestory window uniformly occupies the upper 1,000 mm of the bay, constrained at the base by a 2000 mm-high partial masonry infill wall. Specifically, CASE-1 positions the opening directly adjacent to the left column. This precipitates an acute short-column configuration along the left boundary due to sudden geometric truncation. CASE-2 introduces a 1,000 mm lateral offset from the left column, generating an intermediate frame–infill interaction zone that alters the localized boundary restraint. CASE-3 further translates the opening to a 2000 mm offset, mitigating direct geometric constraints on both vertical load-bearing members. Additionally, CASE-4 mirrors CASE-1 by shifting the opening 3,000 mm from the left, thereby positioning it flush against the right column and transferring the severe localized shear vulnerability to the right boundary.

2.2. Plastic hinges

To rigorously simulate the inelastic seismic response of the RC frame for nonlinear pushover analysis, plastic hinges were assigned to the column and beam based on Table 10-7 (for beams) and Table 10-8 (for columns) in ASCE/SEI 41-13. Given the 2D planar nature of the analytical framework, the plastic hinge definitions are constrained to the M_3 flexural degree of freedom, corresponding to the primary out-of-plane bending about the local 3-axis, while the axial and torsional inelasticities are excluded, ensuring that the structural degradation is governed by primary flexural yielding and subsequent rotational ductility.[25-29] As delineated in **Table 3**, the assigned flexural hinges follow the ASCE/SEI 41-13 force–deformation backbone curve, with Point B (effective yield point) marking baseline flexural yielding at a moment of 384,572.700 kN·mm. Immediate Occupancy (IO), Life Safety (LS), and Collapse Prevention (CP) define discrete performance-level rotation limits of 0.010, 0.025, and 0.050 rad, respectively, corresponding to ultimate flexural capacities of 386,495.56 kN·mm, 401,878.470 kN·mm, and 407,647.060 kN·mm, respectively. Additionally, Points C (ultimate strength point) through E (ultimate failure point) capture post-peak flexural strength degradation and total flexural failure, rather than explicit shear distress.

Adopting the same ASCE/SEI 41-13 methodology, **Table 4** details the beam flexural hinges, with Point B marking the baseline yield moment at 122,796.850 kN·mm, which is approximately one-third of the column capacity. The strength disparity showcases the "strong-column–weak-beam" design philosophy. The joint moment capacity ratio was evaluated under the 1.0DL + 0.5LL load combination, corresponding to an axial demand of $P_u \approx 45$kN. With a column flexural resistance of M_{nc} = 384.57 kN·m and beam capacities of M_{nb}^{+} = 122.80 kN·m and M_{nb}^{-} = 128.94

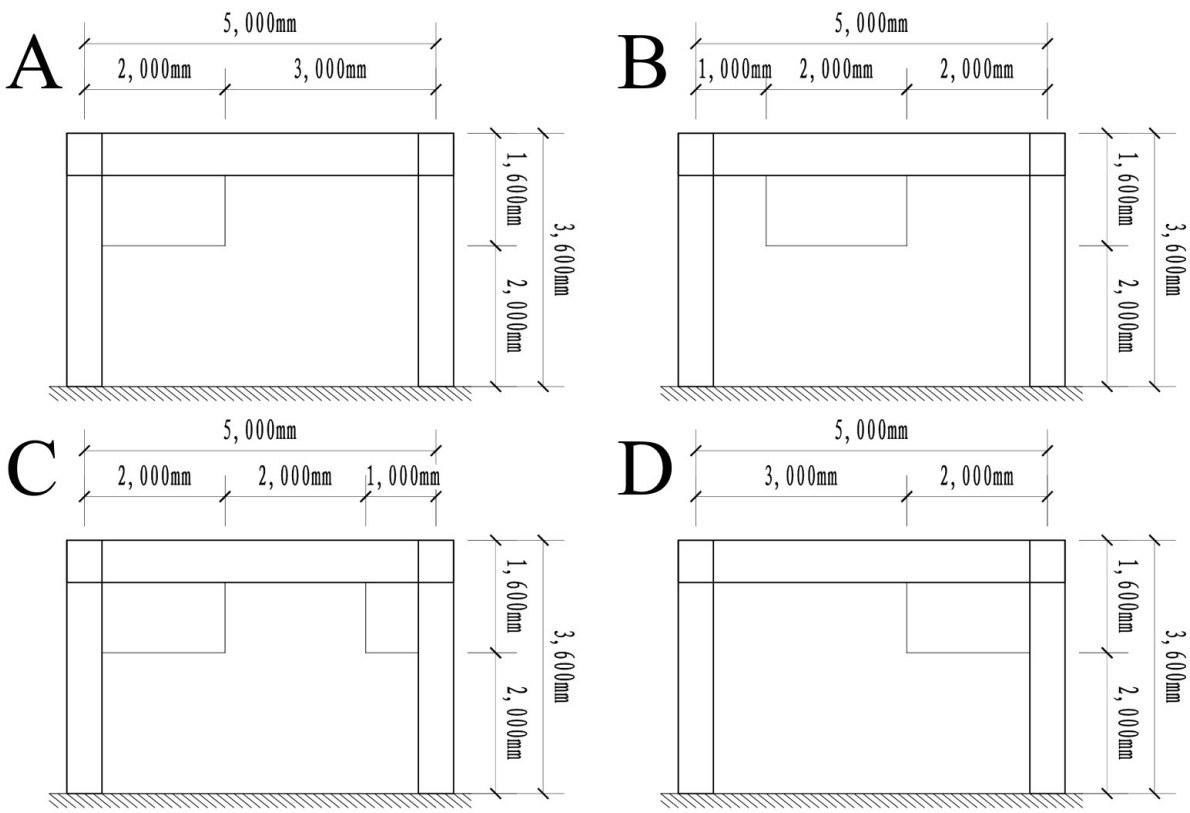

Figure 4. Target infilled one-bay RC frames. (A) CASE-1. (B) CASE-2. (C) CASE-3. (D) CASE-4.
Abbreviation: RC: Reinforced concrete.

kN·m, the calculated strength ratio is $\sum M_{nc} / \sum M_{nb} = 3.05 > 1.2$. According to many previous studies, this design is essential for promoting optimal ductile energy dissipation and averting premature story-mechanism collapse.[30-33] Using identical performance-level rotation limits (0.01, 0.025, and 0.05 rad) as on the column, the IO, LS, and CP states corresponded to ultimate flexural capacities of 124,024.820 kN·m, 125,866.770 kN·m, and 128,936.690 kN·m, respectively.

The corresponding plastic hinge constitutive behaviors generated within the SAP2000 framework are delineated in **Figure 5**, with the Moment/SF versus Rotation/SF curves for the column and beam presented in **Figure 5A** and **5B**, respectively. As depicted in **Figure 5A** and **5B**, the curves adhere to a unified standardized hysteretic envelope characterized by an initial linear-elastic threshold, a defined yielding plateau, progressive plastic strain-hardening, and an ultimate post-peak strength degradation phase.

The flexural capacities dictating the structural response are governed by the member-specific properties synthesized in **Tables 3** and **4**, and are substantiated by the dimensional Yield Moment versus Rotation/SF relationships in **Figures 5C** and **5D**. Driven by its substantially larger cross-sectional geometry and higher longitudinal reinforcement ratio, the RC column exhibited a predefined yield moment of 384,572.700 kN·mm, vastly superseding the beam's yield moment of 122,796.850 kN·mm. According to **Figure 5C**, the progressive accumulation of inelastic rotation corresponds to increasing column ultimate flexural capacities of

Table 3. Plastic hinges on column

Acceptance criteria	Yield moment (kN·mm)	Performance-level rotation limit (rad)	Ultimate flexural capacity at M_3 (kN·mm)
IO	384,572.700	0.010	386,495.560
LS	384,572.700	0.025	401,878.470
CP	384,572.700	0.050	407,647.060

Abbreviations: CP: Collapse Prevention; IO: Immediate Occupancy; LS: Life Safety.

Table 4. Plastic hinges on beam

Acceptance criteria	Yield moment (kN·mm)	Performance-level rotation limit (rad)	Ultimate flexural capacity at M_3 (kN·mm)
IO	122,796.850	0.010	124,024.820
LS	122,796.850	0.025	125,866.770
CP	122,796.850	0.050	128,936.690

Abbreviations: CP: Collapse Prevention; IO: Immediate Occupancy; LS: Life Safety.

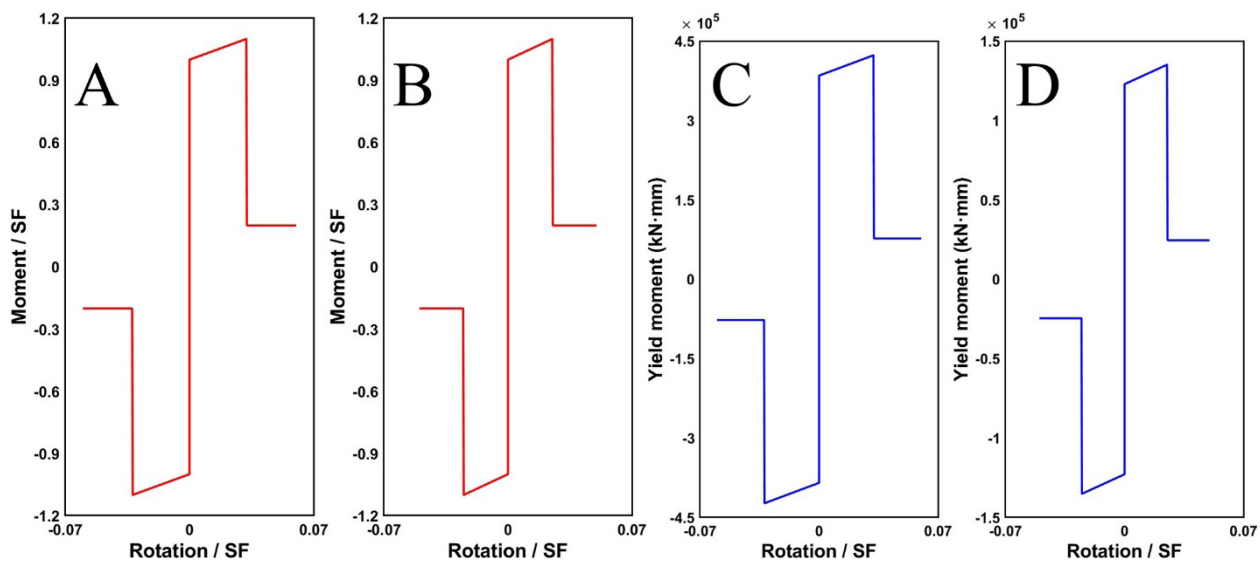

Figure 5. Plastic hinge properties of the column and beam. (A) Column coefficient. (B) Beam coefficient. (C) Column yield moment. (D) Beam yield moment.
Abbreviation: SF: Scale factor.

386,495.560 kN·mm, 401,878.470 kN·mm, and 407,647.060 kN·mm at the IO, LS, and CP thresholds, respectively, as governed by performance-level rotation limits of 0.01, 0.025, and 0.05 rad, respectively. Analogously, the beam hinge's ultimate flexural capacities transitioned from 124,024.820 kN·mm (IO) to 125,866.770 kN·mm (LS) and 128,936.690 kN·mm (CP) under equivalent performance-level rotation limits in **Figure 5D**.

2.3. Nonlinear pushover analysis

Before the nonlinear pushover analysis in this study, a gravity loading protocol comprising dead loads (DL) and live loads (LL) was established to initialize the authentic service-level stress state of the RC frame.[34-36] The derivation of the gravity loads in this study relies on a tributary-area formulation, which is defined by the mathematical expressions depicted in **Equations 2–5** as shown below:

$$P_D = \left(\frac{1}{2} \times W \times \frac{W}{2}\right) \times DL \tag{2}$$

$$\omega_D = \frac{P_D}{L} \tag{3}$$

$$P_L = \left(\frac{1}{2} \times W \times \frac{W}{2}\right) \times LL \tag{4}$$

$$\omega_L = \frac{P_L}{L} \tag{5}$$

where the resultant dead-load force (P_D) transferred to the representative one-bay frame is calculated as the product of the tributary floor area (defined by one-half of the prototype classroom width multiplied by one-half of the transverse tributary width) and the prescribed dead-load intensity (DL), as formulated in **Equation 2**. The corresponding equivalent uniformly distributed DL (ω_D) acting along the RC beam is subsequently derived by dividing P_D by the beam span of L, as expressed in **Equation 3**. Employing an identical tributary methodology, the resultant live-load force (P_L) and its equivalent uniformly distributed LL (ω_L) are quantified using the code-prescribed live-load intensity (LL) via **Equations 4 and 5**, respectively.

To ensure mechanical fidelity and regulatory compliance for educational facilities, the load designs are extracted from the gravity load provisions stipulated in GB 50011. Applying **Equations 2–5**, ω_D imposed on the beam was determined to be 10 kN/m, while the corresponding ω_L was established as 8 kN/m.

Following the previous study by Shi *et al.*[36], ω_D and ω_L of 10 kN/m and 8 kN/m were applied to the representative frame in this study. Additionally, to satisfy the seismic mass participation and load combination mandates stipulated by the GB 50011, the gravity initialization was performed using the seismic load combination below:

$$LC = 1.0 \times DL + 0.5 \times LL \tag{6}$$

To isolate the influence of the clerestory opening positions, the base supports of the vertical load-bearing columns in all four RC frame structures were defined as fully fixed boundary conditions, restraining all translational and rotational degrees of freedom at the ground level. According to Furtado and Rodrigues[37] and Faraji Najarkolaie *et al.*[38], lead–rubber bearing equivalent elements were implemented as localized interfacial dampers simulating the mortar joints between the masonry infill walls and the RC columns to capture the frame–infill interaction, which avoids unrealistic rigid connections that could heavily distort the mechanical analysis. Specifically, the simulated mortar interface in this study was assigned an axial stiffness of 2,100 kN/mm to prevent excessive elemental penetration, while the transverse shear interaction was characterized by a bilinear hysteretic model with an initial elastic stiffness of 10.94 kN/mm and a yield strength of 63 kN. By leveraging these interfacial link properties, the analytical framework replicates the semi-rigid sliding mechanisms of the infill–frame boundary, ensuring a rigorous quantification of the localized short-column effects.

Following gravity load initialization, the displacement-controlled nonlinear pushover analysis was performed to govern the structural response by applying increasing lateral displacement at the control node.[39-41] Specifically, a target displacement of 250 mm was applied at the left node of the top beam across 200 equal incremental steps to capture mechanical transitions from initial elastic behavior to localized yielding and progressive stiffness degradation. Additionally, numerical convergence was achieved via the Newton–Raphson iterative procedure with a force tolerance of 10^{-4}, while accounting for geometric second-order (P–Δ) effects. Based on Guettala *et al.*[42], although recent advancements have produced adaptive and multi-mode pushover methodologies to address higher-mode effects in irregular or tall structures, the primary mode still accounts for over 90% of the total seismic mass participation in the single-story, single-bay RC frame used in this study. Consequently, the adopted displacement-controlled pushover analysis remains valid and effective, despite its static limitations in capturing real-time dynamic spectral variations.

3. Discussion

3.1. Capacity curve

As shown in **Figure 6**, the capacity curves extracted from the nonlinear pushover analyses of the four target RC frames elucidate the evolution of the base shear with structural displacement. Because all target structures share identical geometric parameters, reinforcement detailing, and material constitutive properties, the observed behavioral divergence is only governed by the positioning of the clerestory opening and its subsequent exacerbation of the short-column effect. A fundamental observation from **Figure 6** is the kinematic symmetry between the mirrored configurations: The capacity curves of CASE-1 and CASE-4 (openings adjacent to the left and right boundary columns, respectively) overlap almost perfectly, as do those of CASE-2

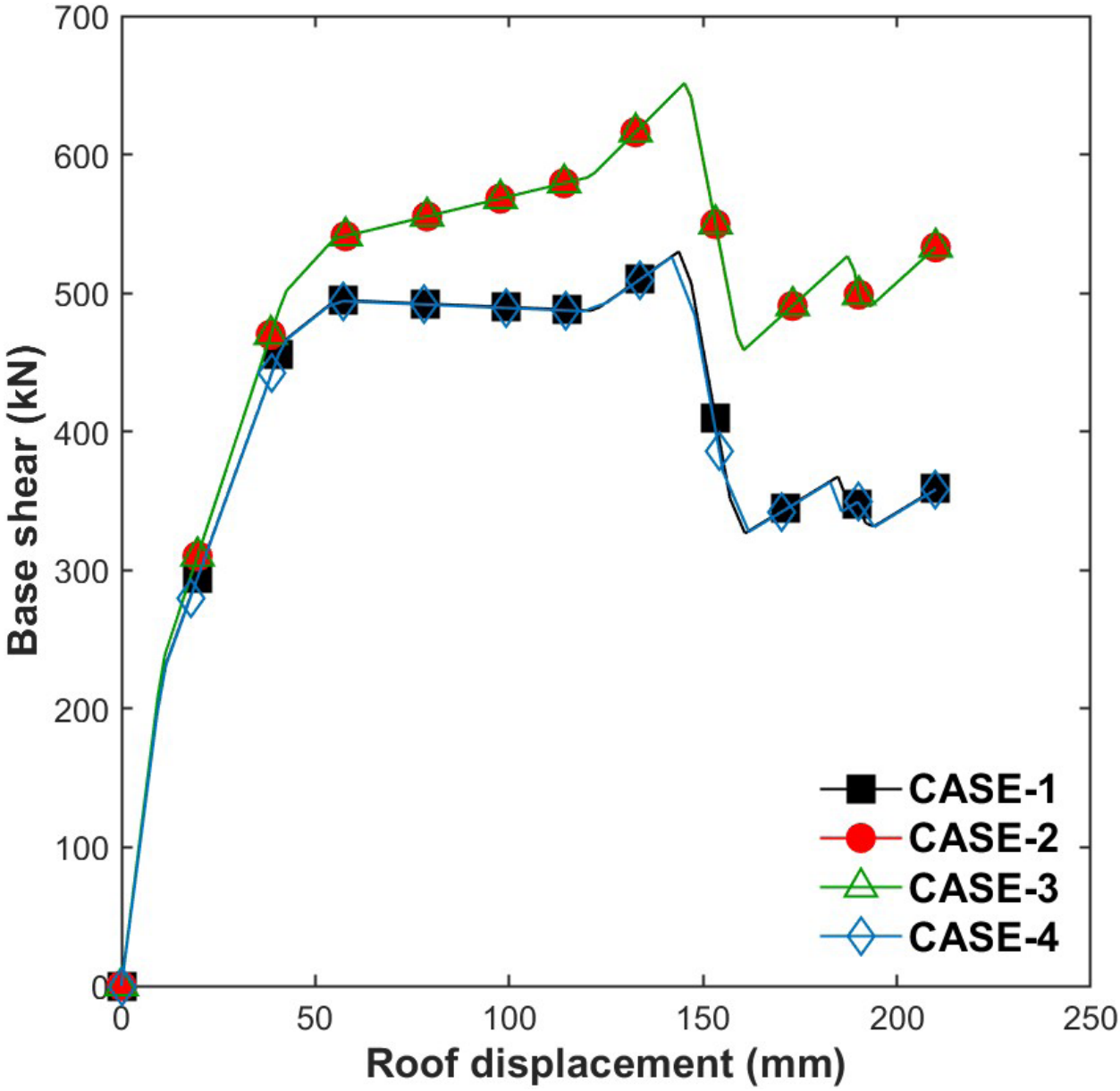

Figure 6. Capacity curve

and CASE-3 (internally offset openings). Rather than the specific loading direction, this geometric congruity validates that the absolute proximity of the clerestory opening to any boundary column is the primary determinant of structural degradation. Although all structures exhibit an initial linear-elastic phase followed by yielding, peak resistance, and post-peak strength degradation, profound disparities emerge in their post-yield trajectories, which underscore that spatial opening arrangements fundamentally alter stiffness redistribution and seismic capacity.

To validate the numerical modeling methodology, the proposed nonlinear pushover analysis was compared against the experimental test data of partially infilled RC frames reported by Hung *et al.*[43] The numerical capacity curves in this study correlate with the experimental test data, reproducing the initial lateral stiffness and peak shear capacity within a 7.5% relative error. Based on the analytical infill RC frame structures in this study, Figure 6 reveals a mechanical dichotomy between boundary-adjacent (CASE-1 and CASE-4) and internally offset (CASE-2 and CASE-3) configurations. When the clerestory opening directly abuts a boundary column, the frame suffers premature stiffness deterioration, entering a prolonged, flat plateau without strain-hardening capacity. Consequently, the average maximum base shear for adjacent configurations (CASE-1: 529.94 kN; CASE-4: 526.04 kN) is reduced substantially by 23.36% compared with that of the non-adjacent structures (CASE-2: 651.28 kN; CASE-3: 651.41 kN), which exhibit stable strain hardening up to their peak capacities. During the post-peak degradation phase (140–150 mm displacement), all structures experienced a base shear drop indicative of severe localized damage. However, CASE-2 and CASE-3 retained a higher residual strength plateau (approximately 500 kN), whereas CASE-1 and CASE-4 plummeted to

approximately 350 kN. As corroborated by Hung *et al.*[43], the post-peak collapse in adjacent configurations indicates a brittle failure mechanism and compromised deformation redundancy.

To evaluate the structural energy absorption capability before failure, the total absorbed energy (W_{abs}) was calculated by integrating the monotonic base shear force $V(x)$ over the lateral displacement trajectory x up to the peak displacement at maximum shear demand (Δ_{peak}), as expressed in **Equation 7**:

$$W_{abs} = \int_0^{\Delta_{peak}} V(x)\,dx \tag{7}$$

where W_{abs} reflects monotonic work absorption rather than cyclic hysteretic energy dissipation. The integrated area under the capacity curve further clarifies the impact of clerestory positioning on the structural system's energy-dissipation capability in this study. As a critical metric for seismic survivability, W_{abs} before reaching the maximum base shear is 62,274.40 J for CASE-1 and 61,254.48 J for CASE-4. Based on the analytical results in **Figure 6**, by translating the opening laterally toward the span interior, the energy absorption capacity surges to 71,486.84 J for CASE-2 and 71,517.61 J for CASE-3, representing an average enhancement of 15.77%, which demonstrates that offsetting the clerestory opening from the primary vertical load-bearing elements mitigates premature, localized damage accumulation. The augmented energy absorption capability of CASE-2 and CASE-3 correlates with the elevated base shear thresholds and sustained post-yield strain hardening, indicating an effective spatial redistribution of internal forces. In contrast, constraints in CASE-1 and CASE-4 localize the inelastic demand, preventing the broader structural system from mobilizing its full monotonic energy absorption capability before structural failure.

From a mechanistic perspective, this pronounced behavioral divergence is entirely dictated by the kinematic interaction between the partial-height masonry infill and the adjacent RC columns.[44-46] In CASE-1 and CASE-4, the masonry panel adjacent to the column acts as a rigid, partial-height lateral restraint, truncating the column's effective deformable length. This constraint forces a "captive column" configuration, triggering a severe localized concentration of shear stress that vastly outpaces flexural yielding. As a result, the RC column fails prematurely in shear, thereby crippling the frame's lateral resistance, as indicated by the sudden drop in the capacity curve and the low base shear in **Figure 6**. Conversely, positioning the clerestory opening toward the interior of the span (CASE-2 and CASE-3) decouples the rigid portion of the infill from the primary boundary columns, alleviating direct geometric truncation, which facilitates a more uniform lateral stiffness distribution, delays the onset of critical plastic hinges, and promotes a ductile, flexure-dominated yielding sequence.

3.2. Performance point

The performance point signifies the theoretical equilibrium coordinate where the structural capacity spectrum intersects the applied seismic demand spectrum, thereby quantifying the anticipated dynamic response of the structure under a specific earthquake.[47-49] Following Shao *et al.*[50], the coordinate is evaluated using the capacity spectrum method within the SAP2000 computational framework, which transforms the nonlinear base shear–roof displacement relationship into acceleration–displacement response spectrum coordinates. For this study, the seismic demand was formulated in accordance with GB 50011 by employing user-defined seismic coefficients of effective peak acceleration coefficient C_a = 0.40 and effective peak velocity coefficient C_v = 0.40 for both the Seismic Evaluation and Retrofit of Concrete Buildings (ATC-40) and Improvement of Nonlinear Static Seismic Analysis Procedures (FEMA 440) assessment protocols.

As detailed in **Tables 5** and **6**, numerical agreement is observed between the performance points derived using the ATC-40 and FEMA 440 procedures across all RC frames. Both evaluations reveal a constant effective damping ratio of 0.05, a uniform spectral acceleration of 1 g, and a structural ductility factor of 1, indicating that the performance point resides within the initial linear-elastic and immediate pre-yield threshold. As such, no significant plastic hysteretic damping is mobilized to trigger the disparate equivalent damping modification algorithms in ATC-40 and FEMA 440. The numerical agreement observed in **Tables 5** and **6** demonstrates the algorithmic consistency of the equivalent linearization procedures in the linear-elastic regime, reflecting a stable, service-level dynamic response. However, this study also emphasizes that this analytical congruence serves to confirm spectrum convergence under identical equilibrium conditions and reflects agreement between two analytical procedures, rather than constituting independent empirical validation of the finite element analysis against experimental results or physical benchmarks.

Although the structural response remains elastic at the performance point, **Tables 5** and **6** reveal kinematic and force disparities governed by clerestory positioning. The infilled RC structures with internally offset openings exhibit superior elastic load-bearing capacities, with CASE-2 and CASE-3 sustaining base shears of 163.833 kN and 163.835 kN, respectively. Conversely, positioning the opening adjacent to boundary columns (CASE-1 and CASE-4) reduces this capacity by 3.48% (158.256 kN and 158.401 kN), yet yields slightly higher roof and spectral displacement demands. CASE-1 and CASE-4 yielded slightly higher roof displacement (Δ) demands (7.413 mm and 7.436 mm, respectively) and spectral displacement (S_d) of 6.286 mm compared to their internally offset counterparts, CASE-2 and CASE-3, which yielded Δ of 7.369 mm and 7.370 mm, respectively, and S_d of 6.227 mm. Correspondingly, the adjacent-column configurations exhibited a prolonged initial effective period (T_{eff}) of 0.159 s relative to CASE-2 and CASE-3 (T_{eff} = 0.158 s). As the pushover analysis progresses in **Figure 7**, the overall elongation of T_{eff} from 0.16 s to 0.55 s acts as an equivalent secant period parameter, calculated as:

Table 5. Performance point (ATC-40)

RC frame	BS (kN)	Δ (mm)	S_a (g)	S_d (mm)	T_{eff} (s)	Ductility (μ)	β_{eff}
CASE-1	158.256	7.413	1.000	6.286	0.159	1.000	0.050
CASE-2	163.833	7.369	1.000	6.227	0.158	1.000	0.050
CASE-3	163.835	7.370	1.000	6.227	0.158	1.000	0.050
CASE-4	158.401	7.436	1.000	6.286	0.159	1.000	0.050

Abbreviations: Δ: Roof displacement; β_{eff}: Effective damping ratio; BS: Base shear; RC: Reinforced concrete; S_a: Spectral acceleration; S_d: Spectral displacement; T_{eff}: Effective period.

Table 6. Performance point (FEMA 440)

RC frame	BS (kN)	Δ (mm)	S_a (g)	S_d (mm)	T_{eff} (s)	Ductility (μ)	β_{eff}
CASE-1	158.256	7.413	1.000	6.286	0.159	1.000	0.050
CASE-2	163.833	7.369	1.000	6.227	0.158	1.000	0.050
CASE-3	163.835	7.370	1.000	6.227	0.158	1.000	0.050
CASE-4	158.401	7.436	1.000	6.286	0.159	1.000	0.050

Abbreviations: Δ: Roof displacement; β_{eff}: Effective damping ratio; BS: Base shear; RC: Reinforced concrete; S_a: Spectral acceleration; S_d: Spectral displacement; T_{eff}: Effective period.

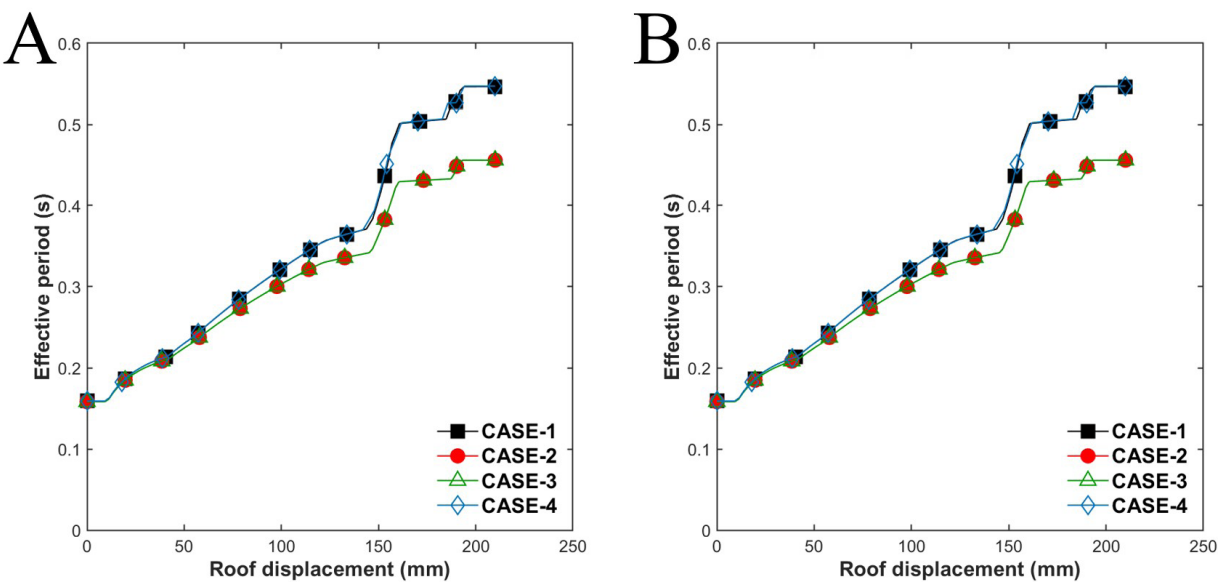

Figure 7. Effective period. (A) ATC-40. (B) FEMA 440.
Abbreviations: ATC-40: Seismic Evaluation and Retrofit of Concrete Buildings; FEMA 440: Improvement of Nonlinear Static Seismic Analysis Procedures.

$$T_{eff} = 2\pi \cdot \sqrt{\frac{M}{K_{sec}}} \tag{8}$$

Based on the calculation in **Equation 8**, this study also emphasizes that the metric functions as a static stiffness-degradation index reflecting the progressive loss of secant lateral rigidity (K_{sec}) due to the short-column effect, rather than a direct nonlinear dynamic vibration record, which confirms that localized geometric truncation compromises frame rigidity even during preliminary seismic excitation.

The capacity–demand spectrum relationships evaluated under the ATC-40 and FEMA 440 equivalent linearization procedures are graphically illustrated in **Figure 8**, with the force–displacement capacity curves obtained from the nonlinear pushover analyses transformed into S_a versus S_d plots. This transformation facilitates a direct graphical comparison with the code-prescribed demand spectra derived from GB 50011, as four demand spectrum curves corresponding to equivalent damping ratios of 5%, 10%, 15%, and 20% are illustrated in **Figure 8A** and **8B**. As shown in **Figure 8**, the capacity spectra of all RC frames intersect the demand spectrum characterized by a 5% damping ratio, and the intersection agrees with the quantitative performance point parameters summarized in **Tables 5**

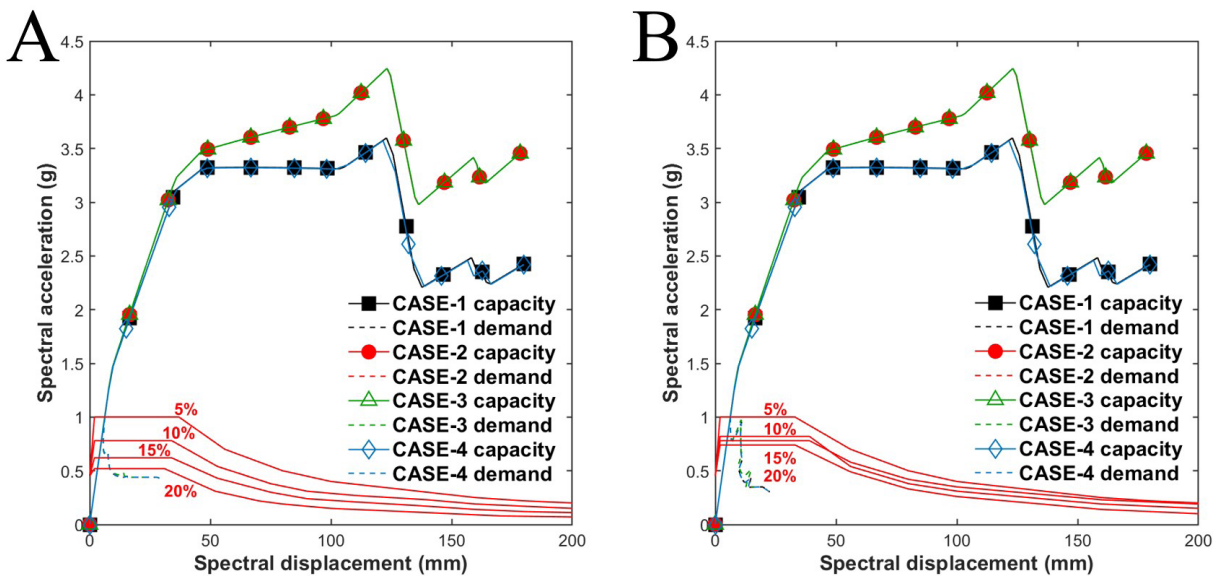

Figure 8. Performance point. (A) ATC-40. (B) FEMA 440.
Abbreviations: ATC-40: Seismic Evaluation and Retrofit of Concrete Buildings; FEMA 440: Improvement of Nonlinear Static Seismic Analysis Procedures.

and **6**, which show an effective damping ratio of exactly 0.05 across all RC structures. The near-perfect alignment of the intersection points at S_a = 1.0 g and S_d ≈ 6.2 mm across both plots in **Figure 8** demonstrates that the equivalent linearization algorithms of ATC-40 and FEMA 440 converge to an identical solution when the structural response remains within the pre-yield or early-yield domain.

For the comparative assessment, the performance-point parameters, including base shear, roof displacement, S_a, S_d, and T_{eff}, were compared among the four RC-frame configurations based on the capacity–demand spectrum relationships obtained using the ATC-40 and FEMA 440 procedures. The comparison further considered differences in the capacity spectra at and beyond the performance point to evaluate the influence of clerestory-opening position on the structural response.

Despite the identical demand profiles, comparison of the capacity spectra in **Figure 8** reveals that the spatial positioning of the clerestory opening governs the post-yield reserve and structural safety of the RC frames. While the initial elastic stiffness trajectories of the four configurations are highly congruent, they diverge significantly in the post-yield region. The capacity spectra for CASE-2 and CASE-3 (internally offset opening configurations) remain consistently and profoundly elevated above those of CASE-1 and CASE-4 (adjacent-column configurations) throughout the entire displacement course of the pushover analysis, which signifies that CASE-2 and CASE-3 maintain a superior spectral acceleration capacity for any given spectral displacement, corroborating the higher base shears, continuous strain hardening, and superior energy dissipation capacities. Conversely, the depressed capacity spectra of CASE-1 and CASE-4 highlight the detrimental influence of the captive-column effect. When the opening abuts a boundary column, premature shear-induced localized damage attenuates the structural capacity spectrum, thereby reducing the structural safety margin (the vertical and horizontal distance between the capacity and demand spectra) beyond the performance point. While all RC frames meet the initial demand spectrum, the larger gap between the capacity and demand curves in CASE-2 and CASE-3 indicates a much more resilient structural system capable of resisting additional seismic demand beyond the initial design level.

The evolution of T_{eff} with increasing Δ is delineated in **Figure 7**, illustrating the trajectories derived from the ATC-40 and FEMA 440 evaluation frameworks, respectively. It characterizes the kinematic degradation response of progressive structural degradation throughout the nonlinear pushover analysis. As shown in **Figure 7A** and **7B**, T_{eff} exhibits a unified, monotonic elongation as lateral displacement increases. This fundamental kinematic behavior reflects the continuous deterioration of the structural lateral stiffness, including concrete cracking, reinforcement yielding, and localized plastic hinge propagation, which lowers the vibration frequency of the RC frame. At the onset of loading, all RC frames initiate with a T_{eff} of approximately 0.16 s, corroborating the elastic-domain performance point values previously shown in **Tables 5** and **6** (0.158–0.159 s). Furthermore, the parity between the ATC-40 and FEMA 440 extends far beyond the initial performance point and produces estimates of dynamic characteristic evolution across the entirety of the inelastic loading procedure.

While all RC frames in this study experience period elongation, a profound kinematic bifurcation materializes

following the onset of severe nonlinear deformation. During the early-to-moderate loading phases (approximately 0 to 140 mm of structural displacement), the T_{eff} of all configurations trace a clustered, increasing path, signifying that initial elastic and early post-yield stiffnesses are primarily influenced by the clerestory opening position. However, coinciding with the severe post-peak capacity drop identified in **Figure 6** (at $\Delta \approx$ 140mm–150 mm), the structural responses diverge. As shown in **Figure 7A** and **7B**, T_{eff} of CASE-1 and CASE-4 (clerestory opening adjacent to the boundary columns) experienced a precipitous surge, plateauing at a highly degraded state of approximately 0.55 s. In contrast, CASE-2 and CASE-3 (internally offset openings) exhibited a significantly restrained period elongation, stabilizing near 0.46 s, which represents a substantial 16% to 20% relative reduction in terminal period elongation. Because T_{eff} is proportional to the square root of structural stiffness, the period elongation observed in CASE-1 and CASE-4 provides a definitive stiffness-degradation indicator of structural rigidity loss triggered by the short-column effect failure mechanism. Conversely, according to the analytical results in CASE-2 and CASE-3, relocating the clerestory opening toward the span's interior averts acute stiffness concentration, fostering a homogeneous distribution of internal forces.

3.3. Plastic hinge stages

As Tidemann and Krenk[51] reported, the initiation and progressive propagation of plastic hinges serve as direct kinematic indicators of structural stiffness deterioration and strength exhaustion during seismic loading. In this study, the evolution of plastic hinges is tracked using the standardized performance-based acceptance criteria defined by ASCE/SEI 41-13. The structural displacement thresholds of the beams corresponding to the critical limit states are summarized in **Table 7**, while the associated deformation at the exact onset of initial yielding is delineated in **Figure 9**. As lateral displacement increased during the nonlinear pushover simulation, all RC frames adhered to a uniform evolutionary sequence, transitioning through the Point B (yielding), IO/LS/CP, and Points C, D, and E (complete structural failure) performance states. **Table 7** reveals a remarkable consistency in the kinematic onset of the states across all structures. Initial plastic yielding (Point B) was consistently triggered within a very narrow displacement band of 9.21 mm to 9.63 mm. Subsequent performance thresholds were closely aligned, with the combined IO/LS/CP limit states clustered near 28 mm, Point C occurring between 53.27 mm and 55.22 mm, and the ultimate failure states (Points D and E) occurring between 107.15 mm and 109.00 mm.

Although the quantitative displacement thresholds exhibit minimal sensitivity to the architectural variations, the structural deformations characterized in **Figure 9** expose a critical and consistent micro-mechanical failure initiation mechanism. Regardless of where the clerestory opening is positioned within the masonry infill (CASE-1 through CASE-4), the incipient plastic hinge invariably localizes at the left end of the RC beam, adjacent to the primary beam–column joint. This consistent spatial concentration identifies the left beam-end as the most vulnerable kinematic nexus of the evaluated one-bay frame during the onset of inelasticity. Mechanistically, this localized vulnerability is caused by the superimposition of pre-existing gravity-induced flexural moments (initialized before pushover) and the local stress concentrations generated by the diagonal compression strut mechanisms mobilized within the masonry infill during lateral displacement.

Synthesizing the plastic hinge initiation metrics with the previously established capacity curves, performance point evaluations, and T_{eff} elongations establishes that optimizing the clerestory opening position provides negligible benefits in artificially delaying the initial onset of structural yielding. Instead, by elevating base shear capacities, enhancing energy dissipation, and stabilizing T_{eff}, the profound structural advantages of isolating the clerestory openings from the boundary columns are exclusively manifested in the post-yield damage propagation phase. In the designs with the clerestory opening abutting the boundary column, the post-yield phase is governed by the short-column effect, intensifying localized shear demands and accelerating stiffness degradation adjacent to the initial yielding zones.

Unlike the beam-end plastic hinges discussed above, the formation of C-stage plastic hinges in the columns signifies that the primary vertical load-carrying members have entered a severe nonlinear damage situation, where the stability of the entire structure becomes vulnerable. The displacement corresponding to each plastic hinge state for the columns is summarized in **Table 8**, while the associated deformations are illustrated in **Figure 10**. Consistent with the beam response, all RC structures in this study exhibited

Table 7. Structural displacement at plastic hinge formation on beams

Performance state	Displacement band (mm)			
	CASE-1	CASE-2	CASE-3	CASE-4
Point B	9.63	9.36	9.36	9.21
IO/LS/CP	27.93	28.02	28.03	28.28
Point C	55.22	53.82	53.80	53.27
Point D	109.00	108.13	108.09	107.15
Point E	109.00	108.13	108.09	107.15

Abbreviations: CP: Collapse Prevention; IO: Immediate Occupancy; LS: Life Safety.

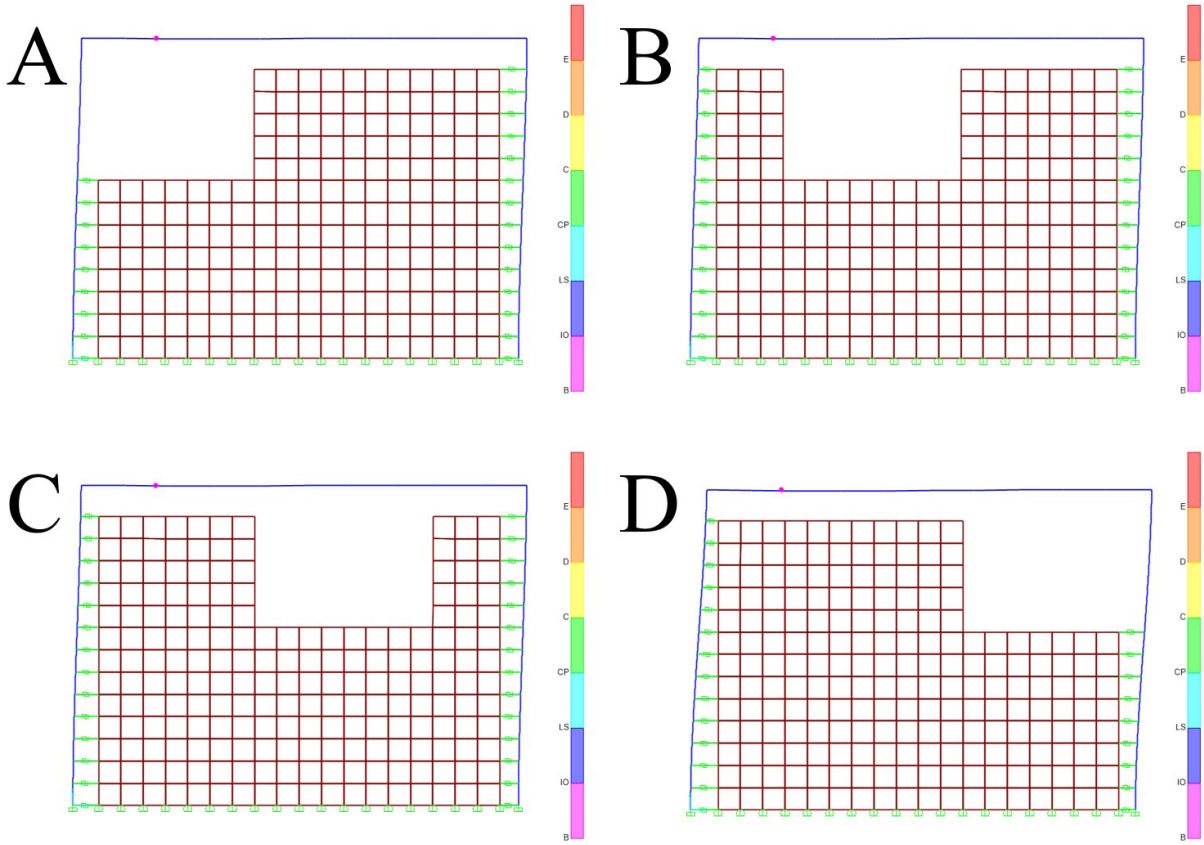

Figure 9. Structural deformation (first plastic hinge formation). (A) CASE-1. (B) CASE-2. (C) CASE-3. (D) CASE-4.
Abbreviations: B: Point B; C: Point C; CP: Collapse Prevention; D: Point D; E: Point E; IO: Immediate Occupancy; LS: Life Safety.

Table 8. Structural displacement at plastic hinge formation on columns

Performance state	Displacement band (mm)			
	CASE-1	CASE-2	CASE-3	CASE-4
Point B	41.73	42.60	42.61	40.67
IO/LS/CP	57.32	57.81	57.83	53.27
Point C	143.74	145.15	145.20	141.97
Point D	156.96	158.71	158.75	155.11
Point E	184.80	187.22	187.25	182.80

Abbreviations: CP: Collapse Prevention; IO: Immediate Occupancy; LS: Life Safety.

the same sequence of hinge evolution (Point B–IO/LS/CP–Point C–Point D–Point E), with substantially larger displacement levels than those observed for the beam hinges. Initial yielding (Point B) occurred at 40.67mm to 42.61 mm, nearly four times greater than the displacement required for the first beam plastic hinge, indicating that the beams serve as the primary energy-dissipation components before column yielding develops. The column plastic hinges subsequently reached the IO/LS/CP stage at approximately 53.27 mm to 57.83 mm, followed by the critical Point C stage at 141.97 mm to 145.20 mm, and the Point D and Point E stages at approximately 155 mm to 159 mm and 183 mm to 187 mm, respectively.

Although the displacement thresholds remain similar among the RC structures in this study, **Figure 10** reveals a distinct difference in the spatial distribution of the first collapse-stage column plastic hinge. In CASE-1, the first column hinge reaching the collapse stage develops at the left column base, whereas in CASE-2, CASE-3, and CASE-4, the first collapse-stage column hinge consistently appears at the right column base. The shift in hinge location reflects the redistribution of lateral stiffness and internal force transfer resulting from different clerestory opening arrangements. For the masonry-infilled RC structure in CASE-1, when the clerestory opening is positioned adjacent to the left boundary column, the short-column effect increases local shear demand and flexural moment concentration

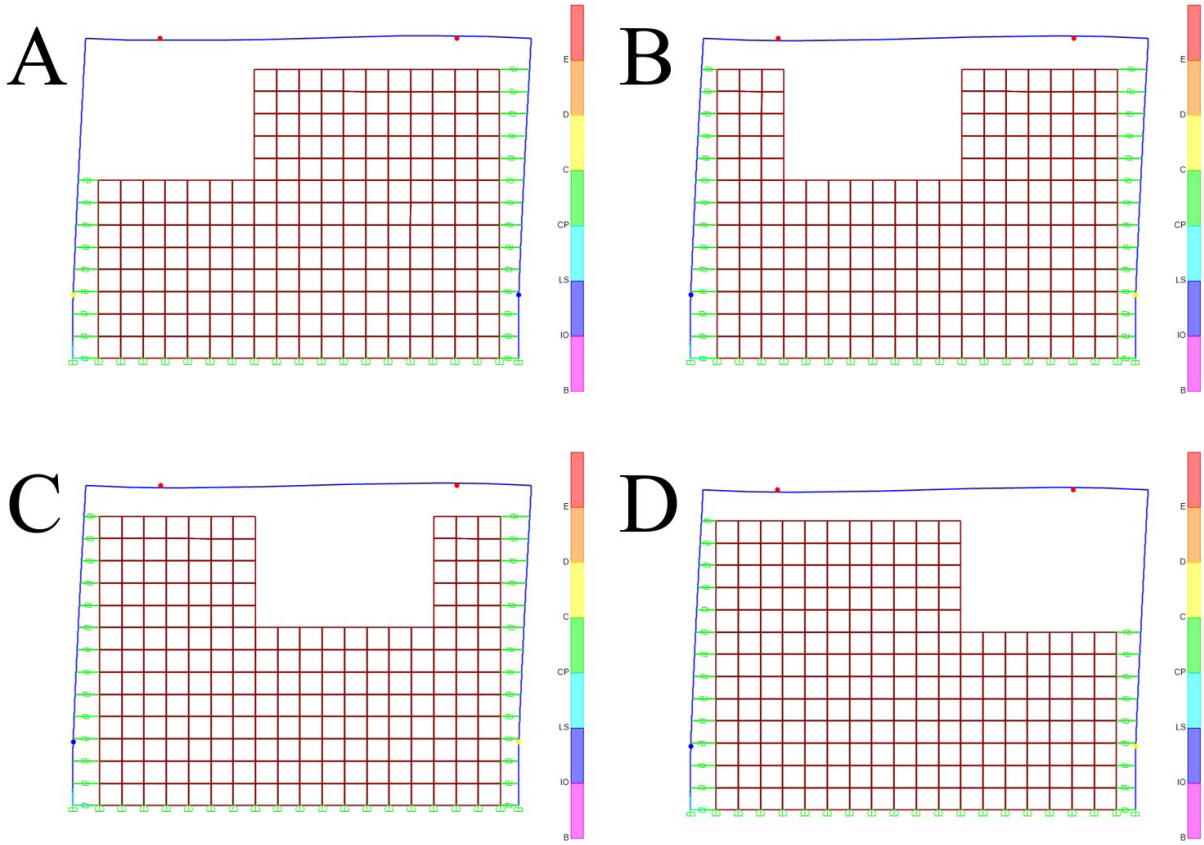

Figure 10. Structural deformation (first plastic hinge formation at the collapse stage of the column). (A) CASE-1. (B) CASE-2. (C) CASE-3. (D) CASE-4.

within the adjacent column, causing nonlinear damage to accumulate at the left column base during progressive lateral loading. Conversely, in CASE-2, CASE-3, and CASE-4, as the clerestory opening is relocated toward the interior span and ultimately adjacent to the right boundary column, the structural stiffness distribution becomes asymmetrical, resulting in a redistribution of overturning moment and base shear toward the opposite side of the frame, causing the critical column yielding location to migrate from the left column base to the right column base.

When the column plastic hinge results are interpreted with the discussed capacity curves, performance-point evaluation, effective-period evolution, and the initial beam plastic hinge formation, a comprehensive understanding of the structural failure mechanism can be established. The beam hinges develop well before the column hinges, confirming that the structural system dissipates seismic energy through flexural yielding of the beams while preserving the integrity of the primary vertical load-resisting members. However, once the displacement approaches 142–145 mm, corresponding to the displacement associated with the maximum base shear observed in the capacity curves, the first collapse-stage column plastic hinge develops, indicating that the structure has entered the critical post-yield stage characterized by rapid stiffness degradation and the onset of structural strength deterioration. When the column plastic hinges achieve the collapse stage, the influence of the clerestory opening becomes pronounced. When the clerestory opening is positioned away from the boundary columns, as in CASE-2 and CASE-3, the largest displacement capacities are achieved before reaching the Point C, D, and E column performance states, with maximum collapse-stage displacements of 145.15 mm and 145.20 mm, respectively. In contrast, when the opening is directly adjacent to a boundary column, as in CASE-1 and CASE-4, the corresponding damage states are achieved at lower collapse-stage displacements (143.74 mm and 141.97 mm, respectively), indicating accelerated damage accumulation induced by the short-column effect. These observations agree with the higher base shear, greater energy dissipation, and reduced T_{eff} elongation observed for CASE-2 and CASE-3, further demonstrating that relocating the clerestory opening away from the boundary columns effectively delays severe column damage, improves post-yield deformation capacity, and enhances the collapse resistance of RC frames subjected to nonlinear seismic loading.

4. Conclusion

This study investigates the nonlinear seismic mechanics of masonry-infilled RC frames incorporating clerestory openings at varying horizontal offsets through nonlinear pushover analysis. Four masonry-infilled RC frames, namely CASE-1, CASE-2, CASE-3, and CASE-4, are formulated to elucidate the structural sensitivity of the short-

column effect, stiffness degradation, energy dissipation, and plastic hinge evolution to different clerestory opening positions. The nonlinear pushover analysis is performed in SAP2000, while adhering to the material and geometric designs of specific Chinese standards and the performance-based evaluation criteria of ASCE/SEI 41-13. Furthermore, capacity–demand equilibrium is evaluated using the equivalent-linearization paradigms of the capacity spectrum method specified in ATC-40 and FEMA 440. By executing a displacement-controlled lateral loading protocol, this analytical framework facilitates a comparative assessment of structural capacities and kinematic failure modes. In conclusion, the computational evidence establishes that the transverse spatial coordinate of a clerestory opening is a critical parameter that redefines the kinematic boundary conditions between the masonry infill and the bounding RC frame, thereby acting as the primary mechanism triggering or mitigating short column-induced localized damage.

Quantitative extraction of the capacity curves demonstrates that the proximity of the clerestory opening to the boundary columns governs the seismic resistance and ductility redundancy. Structural designs where the opening abuts the boundary column (CASE-1 and CASE-4) suffer premature stiffness deterioration caused by acute captive-column constraints. As such, the average maximum base shear capacity of the non-adjacent designs (CASE-2 and CASE-3) exceeds that of the boundary-adjacent designs by 23.36%, coupled with a 15.77% surge in energy dissipation and a 1.62% extension in peak displacement capacity before structural collapse. The results indicate that isolating the clerestory opening toward the interior span is expected to decouple the masonry restraint from the critical vertical load-bearing columns, promoting a uniform redistribution of shear demands. Performance point evaluations further corroborate this finding, as indicated by the convergence of the ATC-40 and FEMA 440 algorithms. This indicates that CASE-2 and CASE-3 preserve greater elastic load-bearing capacity and undergo less T_{eff} elongation than CASE-1 and CASE-4 under identical seismic demand parameters.

The progression of plastic hinge propagation elucidates the localized failure sequences governing the structural collapse of the masonry infilled RC frames. Irrespective of the clerestory opening designs, the initial plastic hinge consistently localized at the left beam end adjacent to the beam–column joint, confirming that initial energy dissipation satisfies the ductile beam-first yielding characteristic of optimal seismic design. However, the subsequent progression of column yielding diverges based on the different structural designs. In RC structures with offset openings (CASE-2 and CASE-3), initiation of column damage (collapse prevention state) is delayed to a higher lateral displacement. Conversely, in column-adjacent masonry infilled RC structures (CASE-1 and CASE-4), the deformable column height triggered post-yield stiffness irregularities, forcing localized shear stress concentrations that accelerated damage propagation at the column base. The findings demonstrate that while the lateral position of the opening does not alter the initiation of structural yielding, it governs the post-yield force transfer trajectories, acting as the catalyst for premature short-column mechanisms and accelerated localized plastic deterioration.

In conclusion, this study demonstrates that the seismic behavior of masonry-infilled RC frames is highly influenced by the spatial relationship between clerestory openings and boundary columns. Isolating openings from column interfaces mitigates short-column effects, improving lateral capacity and structural ductility. While this study provides valuable quantitative insights into how clerestory placement influences localized stiffness degradation, the conclusions are limited to the investigated single-story, single-bay RC frames under nonlinear pushover lateral loading. By producing detailed analytical evidence, this study provides valuable references to subsequent studies on multi-story, multi-bay RC structures.

Acknowledgments

This work benefited significantly from the comprehensive resources provided by the Ankang Science & Technology Innovation Center (Qinchuangyuan Platform), which offered technical assistance and facilitated this scientific investigation.

Funding

This work was supported by the 25th Batch High-Level Talent Research Project of Ankang University, "Seismic Response and Collapse Mechanisms of RC Structures via Deep Learning–Finite Element Coupling," under the Grant 2026AYQDZR27.

Conflict of interest

The authors declare they have no competing interests.

Author contributions

Conceptualization: Mo Shi, Yeol Choi
Data curation: Mo Shi
Formal analysis: Mo Shi
Investigation: Mo Shi, Xinyue Cu
Methodology: Mo Shi
Project administration: Mo Shi
Resources: Mo Shi, Xinyue Cu
Software: Mo Shi
Supervision: Mo Shi, Yeol Choi
Validation: Mo Shi, Yeol Choi
Visualization: Mo Shi
Writing–original draft: Mo Shi
Writing–review & editing: Mo Shi

Availability of data

None.

AI tools statement

All authors confirm that no AI tools were used in the preparation of this manuscript.

References

1. Fujii K. Seismic response of reinforced concrete

moment-resisting frame with steel damper columns under earthquake sequences: evaluation using extended critical pseudo-multi impulse analysis. *Front Built Environ*. 2025;11:1561534.

https://doi.org/ 10.3389/fbuil.2025.1561534

2. Oyguc R, Aygun ZS, Oyguc E. Fragility of irregular RC buildings under mainshock-aftershock sequences. *Bull Earthquake Eng*. 2026.

https://doi.org/ 10.1007/s10518-026-02537-2

3. Li SQ, Beer M, Gardoni P. Probabilistic seismic risk and vulnerability assessment framework for RC buildings considering the influence of mainshock-aftershock sequences. *Prob Eng Mech.* 2026;84:103921.

https://doi.org/ 10.1016/j.probengmech.2026.103921

4. Cavuslu M, Agace BT, Ülger T. Seismic failure mechanisms of a reinforced-concrete minaret with stair-core discontinuities: field evidence, experimental insights, and 3D nonlinear analysis. *Eng Fail Anal*. 2026;191:110790.

https://doi.org/ 10.1016/j.engfailanal.2026.110790

5. Tamizharasi G. Evaluating earthquake resilience: Strategies for mitigating short column effects in reinforced concrete buildings through energy-based damage assessment. *Struct Concr*. 2026;27(2):2197–2215.

https://doi.org/ 10.1002/suco.70451

6. Cagatay IH, Beklen C, Mosalam KM. Investigation of short column effect of RC buildings: failure and prevention. *Comput Concr*. 2010;7(6):523–532.

https://doi.org/ 10.12989/cac.2010.7.6.523

7. Duran B, Tunaboyu O, Avsar O. Structural failure evaluation of a substandard RC building due to basement story short-column damage. *J Perform Constr Facil*. 2020;34(4):04020053.

https://doi.org/ 10.1061/(ASCE)CF.1943-5509.0001455

8. Arcuri D, Petrini L, Mihaylov BI. Three-parameter kinematic theory for shear assessment of reinforced concrete short columns. *Struct Concr*. Published online July 11, 2026.

https://doi.org/ 10.1002/suco.70704

9. Zhang S, Guo L, Ge L, Wang E, Tong J. Performance-based seismic evaluation of local staggered RC frames with steel tube-reinforced concrete columns under multi-angle earthquakes. *Appl Sci*. 2025;15(16):9092.

https://doi.org/ 10.3390/app15169092

10. Zhang J, Lata A, Guo X, Xu Z. Seismic vulnerability assessment of reinforced concrete school buildings based on the concept of balanced seismic shear force distribution. *Structures*. 2025;71:108184.

https://doi.org/ 10.1016/j.istruc.2024.108184

11. Hammad A, Akbarnezhad A, Grzybowska H, Wu P, Wang X. Mathematical optimisation of location and design of windows by considering energy performance, lighting and privacy of buildings. *Smart Sustain Built Environ*. 2019;8(2):117–137.

https://doi.org/ 10.1108/SASBE-11-2017-0070

12. Ou YC, Nguyen NVB, Hoang L. Cyclic behavior and pushover analysis of large scale two-bay, two-story reinforced concrete frames infilled with walls with openings. *Eng Struct*. 2024;317:118663.

https://doi.org/ 10.1016/j.engstruct.2024.118663

13. Maidiawati, Tanjung J, Hayati Y, Ridwan M, Masdar A. Seismic performance of masonry partially infilled RC frame based on numerical analysis applying strut model. *Int J GEOMATE*. 2025;29(134):32–40.

https://doi.org/ 10.21660/2025.134.4856

14. Han SW, Lee CS. Cyclic behavior of lightly reinforced concrete moment frames with partial- and full-height masonry walls. *Earthq Spectra*. 2020;36(2):599–628.

https://doi.org/ 10.1177/8755293019899960

15. Han Y, Han JP, Yu XH. Energy-based state-dependent fragility of RC frame structures with infilled walls subjected to mainshock-aftershock sequences. *J Build Eng*. 2026;117:114827.

https://doi.org/ 10.1016/j.jobe.2025.114827

16. Han Y, Han J, Huang L. Mainshock–aftershock fragility analysis of RC structures considering IP-OOP interaction of infill masonry walls. *KSCE J Civ Eng*. 2024;28(9):3873–3890.

https://doi.org/ 10.1007/s12205-024-2044-x

17. Furtado A, Rodrigues H, Varum H, Arêde A. Mainshock-aftershock damage assessment of infilled RC structures. *Eng Struct*. 2018;175:645–660.

https://doi.org/ 10.1016/j.engstruct.2018.08.063

18. Sung YC, Lin TK, Hsiao CC, Lai MC. Pushover analysis of reinforced concrete frames considering shear failure at beam-column joints. *Earthq Eng Eng Vib*. 2013;12(3):373–383.

https://doi.org/ 10.1007/s11803-013-0179-8

19. Su RKL, Tang TO, Lee CL. Evaluation of local and global ductility relationships for seismic assessment of regular masonry-infilled reinforced concrete frames using the coefficient-based method. *Earthq Struct*. 2013;5(1):1–22.

https://doi.org/ 10.12989/eas.2013.5.1.001

20. Li S, Zuo Z, Zhai C, Xie L. Comparison of static pushover and dynamic analyses using RC building shaking table experiment. *Eng Struct*. 2017;136:430–440.

https://doi.org/ 10.1016/j.engstruct.2017.01.033

21. Azadi Kakavand MR, Neuner M, Schreter M, Hofstetter G. A 3D continuum FE-model for predicting the nonlinear response and failure modes of RC frames in pushover analyses. *Bull Earthquake Eng*. 2018;16(10):4893–4917.

https://doi.org/ 10.1007/s10518-018-0388-7

22. Sullivan TJ, Saborio-Romano D, O'Reilly GJ, Welch DP, Landi L. Simplified pushover analysis of moment resisting frame structures. *J Earthq Eng*. 2021;25(4):621–648.

https://doi.org/ 10.1080/13632469.2018.1528911

23. Fragiadakis M, Vamvatsikos D, Aschheim M. Application of nonlinear static procedures for the seismic assessment of regular RC moment frame buildings. *Earthq Spectra*. 2014;30(2):767–794.

https://doi.org/ 10.1193/111511EQS281M

24. Youssef MA, Elfeki MA. Predicting local seismic damage of RC framed buildings considering the horizontal seismic component. *Mag Concr Res*. 2013;65(23):1411–1428.

https://doi.org/ 10.1680/macr.13.00156

25. Arroyo O, Barros J, Ramos L. Comparison of the reinforced-concrete seismic provisions of the design codes of the United States, Colombia, and Ecuador for low-rise frames. *Earthq Spectra*. 2018;34(2):441–458.

https://doi.org/ 10.1193/102116EQS178EP

26. Ranjith A, Kiran BM, Sanjith J, Mahesh Kumar CL, Shwetha KG. Performance based seismic analysis of RC structural system under earthquake excitation. *Int J Adv Technol Eng Explor*. 2022;9(91):735–758.

https://doi.org/ 10.19101/IJATEE.2021.875292

27. Raju KR, Cinitha A, Iyer NR. Seismic performance evaluation of existing RC buildings designed as per past codes of practice. *Sadhana*. 2012;37(2):281–297.

https://doi.org/ 10.1007/s12046-012-0080-6

28. Birely AC, Lowes L, Lehman DE. A model for the practical nonlinear analysis of reinforced-concrete frames including joint flexibility. *Eng Struct*. 2012;34:455–465.

https://doi.org/ 10.1016/j.engstruct.2011.09.003

29. Makarios TK, Bakalis AP, Ntaliakouras I, Karayannis CG. The hybrid "M and P" technique for seismic damage identification in planar dual reinforced concrete frames. *Soil Dyn Earthq Eng*. 2025;194:109344.

https://doi.org/ 10.1016/j.soildyn.2025.109344

30. Zhang C, Tao MX. Strong-column–weak-beam criterion for reinforced concrete frames subjected to biaxial seismic excitation. *Eng Struct*. 2021;241:112481.

https://doi.org/ 10.1016/j.engstruct.2021.112481

31. Li F, Li Y, Luo W, Lei C, Pan W, Ji S. A new seismic strategy for strong column-weak beam design philosophy in RC frame structures. *Structures*. 2025;77:109129.

https://doi.org/ 10.1016/j.istruc.2025.109129

32. Zuo Z, Gong M, Sun J, Zhang H. Seismic performance of RC frames with different column-to-beam flexural strength ratios under the excitation of pulse-like and non-pulse-like ground motion. *Bull Earthquake Eng*. 2021;19(1):5139–5159.

https://doi.org/ 10.1007/s10518-021-01159-0

33. Ghorbanzadeh M, Khoshnoudian F. The effect of strong column-weak beam ratio on the collapse behaviour of reinforced concrete moment frames subjected to near-field earthquakes. *J Earthq Eng*. 2022;26(8):4030–4053.

https://doi.org/ 10.1080/13632469.2020.1822228

34. Scalvenzi M, Gargiulo S, Freddi F, Parisi F. Impact of seismic retrofitting on progressive collapse resistance of RC frame structures. *Eng Fail Anal*. 2022;131:105840.

https://doi.org/ 10.1016/j.engfailanal.2021.105840

35. Dadi VSK, Agarwal P. Updating of nonlinear analytical modeling of soft storey RC frame building models based on cyclic test results. *Bull Earthquake Eng*. 2013;11(5):1493–1515.

https://doi.org/ 10.1007/s10518-013-9434-7

36. Shi M, Choi Y. Nonlinear pushover analysis of the mechanical influences under the varied stories and column orientations in RC structures. *Insight Civ Eng*. 2024;7(1):610.

https://doi.org/ 10.18282/ice.v7i1.610

37. Furtado A, Rodrigues H. Simplified macro-model for non-interactive masonry infill walls. *J Earthq Eng*. Published online June 15, 2026.

https://doi.org/ 10.1080/13632469.2026.2685685

38. Faraji Najarkolaie K, Mohammadi M, Fanaie N. Realistic behavior of infilled steel frames in seismic events: experimental and analytical study. *Bull Earthquake Eng*. 2017;15:5365–5392.

https://doi.org/ 10.1007/s10518-017-0173-z

39. Shahriar MS, Amanat KM. Investigation on collapse mechanism of soft ground storied buildings at different locations of Bangladesh based on pushover analysis. *Structures*. 2025;79:109620.

https://doi.org/ 10.1016/j.istruc.2025.109620

40. Abd-Elhamed A, Mahmoud S, Alotaibi KS. Nonlinear analysis of reinforced concrete buildings with different heights and floor systems. *Sci Rep*. 2023;13:14949.

https://doi.org/ 10.1038/s41598-023-41656-7

41. Chandrasekaran S, Pachaiappan S. Displacement-controlled nonlinear analysis of offshore platform topside under accidental loads. *Arab J Sci Eng*. 2023;48(4):5619–5635.

https://doi.org/ 10.1007/s13369-022-07509-7

42. Guettala S, Abdesselam I, Rahmani AY, Khelaifia A, Guettala S. Advancements in pushover analysis for improved seismic performance evaluation. *Arch Comput Methods Eng*. 2025;32(7):4525–4554.

https://doi.org/ 10.1007/s11831-025-10278-9

43. Hung CC, Wang YQ, Yen CH. Retrofitting of masonry-infilled RC frames using UHPC shotcrete: full-scale experiments and strength modeling. *Constr Build Mater*. 2026;537:146982.

https://doi.org/ 10.1016/j.conbuildmat.2026.146982

44. Mohammad AF, Faggella M, Gigliotti R, Spacone E. Seismic performance of older R/C frame structures accounting for infills-induced shear failure of columns. *Eng Struct*. 2016;122:1–13.

https://doi.org/ 10.1016/j.engstruct.2016.05.010

45. Zhou X, Kou X, Peng Q, Cui J. Influence of infill wall

configuration on failure modes of RC frames. *Shock Vib*. 2018;2018:6582817.

https://doi.org/ 10.1155/2018/6582817

46. Pradhan PM, Maskey RK, Pradhan PL. Stiffness behavior and shear effect in partially infilled reinforced concrete frames. *J Earthq Eng*. 2014;18(4):580–588.

https://doi.org/ 10.1080/13632469.2013.873373

47. Cinitha A, Umesha PK, Iyer NR, Lakshmanan N. Performance-based seismic evaluation of RC framed building. *J Inst Eng India Ser A*. 2015;96(4):285–294.

https://doi.org/ 10.1007/s40030-015-0129-8

48. Thomos GC, Trezos CG. Examination of the probabilistic response of reinforced concrete structures under static non-linear analysis. *Eng Struct*. 2006;28(1):120–133.

https://doi.org/ 10.1016/j.engstruct.2005.08.003

49. Bhandari M, Bharti SD, Shrimali MK, Datta TK. Applicability of capacity spectrum method for base-isolated building frames at different performance points. *J Earthq Eng*. 2021;25(2):270–299.

https://doi.org/ 10.1080/13632469.2018.1515795

50. Shao JH, Gu Q, Shen YK. Seismic performance evaluation of steel frame-steel plate shear walls system based on the capacity spectrum method. *J Zhejiang Univ Sci A*. 2008;9(3):322–329.

https://doi.org/ 10.1631/jzus.A071285

51. Tidemann L, Krenk S. Cyclic plastic hinges with degradation effects for frame structures. *J Eng Mech*. 2017;143(12):04017142.

https://doi.org/ 10.1061/(ASCE)EM.1943-7889.0001358